Toward a Local Explicit Parabolized Stability Solver for High-Speed Flows

Christian B. King* and Steven A. E. Miller†
University of Florida, Gainesville, Florida, 32611

A new explicit, locally filtering, parabolized stability solver is being developed for hypersonic shear and boundary layers. This explicit approach, named Characteristic-filtering And One-way Stability solver (CHAOS), has the potential to predict turbulent transition onset, heat transfer, skin-friction drag, and unsteady loading at a low computational expense for vehicle designers. Currently, CHAOS is validated for uniform subsonic and supersonic base flows and is shown to be well-suited for spatial integration, with upstream-traveling characteristics removed to ensure a well-posed system in subsonic base flow. Results are presented for one- and two-dimensional acoustic waves in a stationary medium, demonstrating agreement within one percent between predicted real pressure perturbations.

Nomenclature

$\boldsymbol{A}$	=	streamwise LNS Jacobian
$\boldsymbol{B}$	=	cross-flow LNS Jacobian
$\boldsymbol{C}$	=	source term Jacobian
$\boldsymbol{D}$	=	diffusive LNS Jacobian
f	=	frequency
$\mathcal{F}$	=	Fourier transform operator
i	=	imaginary number
k	=	wavenumber
M	=	Mach number
$\boldsymbol{q}$	=	fluid solution vector
R_1	=	effective radius from acoustic source
u	=	streamwise velocity
v	=	cross-flow velocity
p	=	pressure
x, y	=	rectangular coordinates
υ	=	specific volume
γ	=	ratio of specific heats
γ_k	=	Prandtl-Glauert factor
$\boldsymbol{\psi}$	=	spatial discretization matrix
$\boldsymbol{\phi}$	=	characteristic solution vector
ω	=	angular frequency
$\overline{\square}$	=	time average quantity
$\square'$	=	fluctuating quantity
$\hat{\square}$	=	Fourier transformed fluctuating quantity
$\square_\infty$	=	freestream quantity

I. Introduction

The understanding of instability and turbulent transition in the hypersonic regime is crucial for improving the performance and safety of hypersonic flight-vehicles. Spatial marching stability solvers allow for predictions

*Ph.D. Candidate, National Science Foundation Graduate Research Fellow, Department of Mechanical and Aerospace Engineering, christianking@ufl.edu, AIAA student member.

†DARPA Director's Fellow and Associate Professor of Mechanical and Aerospace Engineering, Theoretical Fluid Dynamics and Turbulence Group, Department of Mechanical & Aerospace Engineering, University of Florida, 413 NEB, P. O. Box 116250, Gainesville, FL 32611, saem@ufl.edu; saemiller@gmail.com, AIAA Associate Fellow and lifetime member.

at a greatly reduced computational expense [1–4]. The current state of the art in spatial-marching stability solvers either makes excessive assumptions on solution shape in order to stabilize the integration method, or does not include high-order, optimal discretization schemes for the propagation of acoustic waves. We address this issue by introducing a high-order parabolized stability solver. High order, dispersion relation preserving discretization is employed for optimal propagation of acoustic waves, which are dominant in second-mode hypersonic instability [5].

The linear Parabolized Stability Equations (PSE) spatially march governing equations downstream to predict the evolution of stability waves. However, classical linear stability theory (LST) utilizes the parallel flow assumption, which eliminates terms associated with base flow variation along the streamwise direction along with base flow velocities in cross-stream directions [6]. PSE does not have this limitation, but requires a minimum step-size for damping of upstream traveling disturbances [1, 7]. Both approaches assume the shape of the disturbances, which preclude the prediction of multi-modal wave interactions [1]. The Euler and One-Way Navier-Stokes (OWNS) approaches of Towne and Colonius [8], Rigas et al. [9], Zhu and Towne [10], and Towne et al. [11] overcome these limitations by parabolizing the governing equations with high-order recursive filters.

Bertolotti et al. [12] utilized PSE to investigate the downstream evolution of Tollmien-Schlichting waves in laminar boundary layers and showed that non-parallel effects are small when cross-stream velocity components are non-zero. The PSE are a useful tool for analyzing the transient growth of disturbances for the prediction of transition in nominally stable or weakly unstable boundary layers. Paredes et al. [13] used the linear form of PSE to study the algebraic disturbance growth in compressible boundary layers and found that a favorable pressure gradient weakens the maximum energy gain near a planar stagnation point. Paredes et al. [14] also expanded this work into three dimensions with discretized wall-normal derivatives using the high-order scheme of Hermanns and Hernandez [15]. The relation between spatial growth and temporal growth of disturbances was shown by Gaster [16] with solutions of the Orr-Sommerfeld equation. Gaster [17] later showed that singular points exist in the eigenvalues of downstream traveling modes and that modes corresponding to zero base flow group velocity decay in time.

We present a new Characteristic-filtering And One-way Stability solver (CHAOS) based on the methodology of Towne et al. [11], Towne and Colonius [8], and Rigas et al. [18]. Towne et al. [11] parabolized the governing equations by filtering upstream traveling modes with a recursive approximation of the eigenvalues of the discretization matrix at the succeeding marching plane. The presented approach differs by not computing eigenvalues of the discretization matrix at each integration plane. This new approach is explicit in the streamwise direction and requires a direct local calculation of upstream traveling characteristics based on diagonalization of the streamwise linearized Navier-Stokes (LNS) Jacobian. The main reason for choosing this approach is to continuously increase the order of integration in the streamwise direction due to the explicit parabolization of the current marching plane.

Section II outlines the equations solved, the details of the numerical solver, and the upstream characteristic filtering algorithm. Section III presents aeroacoustic validation cases for subsonic and supersonic stationary base flows. Section IV summarizes the new method introduced, results, and outlines target applications for future work.

II. Methodology

We present the methodology of the CHAOS code, beginning with the Navier-Stokes (NS) equations. The NS equations are decomposed via Reynolds averaging and the resulting equations are Fourier transformed in time. The equations are transformed into characteristic space via the streamwise LNS Jacobian and a filtering algorithm is applied in local subsonic flow to make the equations well-posed for streamwise spatial integration.

A. Governing Equations

The Navier-Stokes (NS) equations and conservation of energy with an ideal gas closure govern the flow-field. Terms associated with a statistically stationary base flow are retained. The LNS equations, with zero streamwise viscosity gradients, conserve perturbations about a base flow in mass, streamwise momentum, cross-flow momentum, and energy. These equations are expressed as

$$\frac{\partial \boldsymbol{q}'}{\partial t} + \boldsymbol{A}\frac{\partial \boldsymbol{q}'}{\partial x} + \boldsymbol{B}\frac{\partial \boldsymbol{q}'}{\partial y} + \boldsymbol{C}\boldsymbol{q}' + \boldsymbol{D}\frac{\partial^2 \boldsymbol{q}'}{\partial y^2} = \boldsymbol{0}, \tag{1}$$

where $\boldsymbol{q}' = [\upsilon', u', v', p']^T$, p is static pressure, u and v are velocity components, and υ is the specific volume. Matrices $\boldsymbol{A}$, $\boldsymbol{B}$, $\boldsymbol{C}$, and $\boldsymbol{D}$ in two dimensions, are defined as

$$
\boldsymbol{A} = \begin{bmatrix} \overline{u} & \overline{\upsilon} & 0 & 0 \\ 0 & \overline{u} & 0 & \overline{\upsilon} \\ 0 & 0 & \overline{u} & 0 \\ 0 & \gamma\overline{p} & 0 & \overline{u} \end{bmatrix}, \tag{2}
$$

$$
\boldsymbol{B} = \begin{bmatrix} \overline{v} & \overline{\upsilon} & 0 & 0 \\ 0 & \overline{v} & 0 & 0 \\ 0 & 0 & \overline{u} & \overline{\upsilon} \\ 0 & 0 & \gamma\overline{p} & \overline{v} \end{bmatrix}, \tag{3}
$$

$$
\boldsymbol{C} = \begin{bmatrix} -\nabla\cdot\overline{\boldsymbol{u}} & \frac{\partial\overline{\upsilon}}{\partial x} & \frac{\partial\overline{\upsilon}}{\partial y} & 0 \\ \frac{\partial\overline{p}}{\partial x} - \frac{1}{\mathrm{Re}}\nabla^2\overline{u} & \frac{\partial\overline{u}}{\partial x} & \frac{\partial\overline{u}}{\partial y} & 0 \\ \frac{\partial\overline{p}}{\partial y} - \frac{1}{\mathrm{Re}}\nabla^2\overline{v} & \frac{\partial\overline{v}}{\partial x} & \frac{\partial\overline{v}}{\partial y} & 0 \\ -\frac{\gamma}{\mathrm{RePr}}\nabla^2\overline{p} & \frac{\partial\overline{p}}{\partial x} & \frac{\partial\overline{p}}{\partial y} & \gamma\nabla\cdot\overline{\boldsymbol{u}} - \frac{\gamma}{\mathrm{RePr}}\nabla^2\overline{\upsilon} \end{bmatrix}, \tag{4}
$$

and

$$
\boldsymbol{D} = \begin{bmatrix} 0 & 0 & 0 & 0 \\ 0 & -\frac{\overline{\upsilon}}{\mathrm{Re}} & 0 & 0 \\ 0 & 0 & -\frac{\overline{\upsilon}}{\mathrm{Re}} & 0 \\ -\frac{\gamma\overline{p}}{\mathrm{RePr}} & 0 & 0 & -\frac{\gamma\overline{\upsilon}}{\mathrm{RePr}} \end{bmatrix}. \tag{5}
$$

Here, Pr is the Prandtl number, Re and γ is the ratio of specific heats. The operators, $\overline{\square}$ and $\square'$ indicate ensemble averaged base flow and perturbation variables, respectively.

Frequency domain techniques have significant advantages [7, 8, 11]. These include reduced computational cost and isolation of particular important angular frequencies, ω. The Fourier transform is defined as

$$
\mathcal{F}(\varphi) = \hat{\varphi} = \frac{1}{2\pi}\int_{-\infty}^{\infty} \varphi \exp(i\omega t)dt, \tag{6}
$$

where $\mathcal{F}()$ is the Fourier transform operator and φ is the transformed variable. It is noted that for the time derivative of fluid variables, $\boldsymbol{q}$ that

$$
\mathcal{F}\left(\frac{\partial\boldsymbol{q}'}{\partial t}\right) = -i\omega\hat{\boldsymbol{q}}. \tag{7}
$$

The Fourier transform is applied to Eqn. (1) and has the form

$$
\boldsymbol{A}\frac{d\hat{\boldsymbol{q}}}{dx} = i\omega\hat{\boldsymbol{q}} - \boldsymbol{B}\frac{\partial\hat{\boldsymbol{q}}}{\partial y} - \boldsymbol{C}\hat{\boldsymbol{q}} - \boldsymbol{D}\frac{\partial^2\hat{\boldsymbol{q}}}{\partial y^2}, \tag{8}
$$

where $\hat{\square}$ indicates Fourier-transformed perturbation variables.

The goal is to spatially march these equations in the streamwise direction. Therefore, derivatives with respect to x are isolated on the left-hand side. The resultant equations, in expanded form, are

$$
\frac{\partial\hat{\upsilon}}{\partial x} = \frac{1}{\overline{u}}\left[i\omega\hat{\upsilon} + \overline{\upsilon}\frac{\partial\hat{u}}{\partial x} - \overline{v}\frac{\partial\hat{\upsilon}}{\partial y} + \overline{\upsilon}\frac{\partial\hat{v}}{\partial y} + \hat{\upsilon}\left(\frac{\partial\overline{u}}{\partial x} + \frac{\partial\overline{v}}{\partial y}\right) - \hat{u}\frac{\partial\overline{\upsilon}}{\partial x} - \hat{v}\frac{\partial\overline{\upsilon}}{\partial y}\right], \tag{9}
$$

$$
\frac{\partial\hat{u}}{\partial x} = \frac{1}{\overline{u}}\left[i\omega\hat{u} - \overline{\upsilon}\frac{\partial\hat{p}}{\partial x} - \overline{v}\frac{\partial\hat{u}}{\partial y} - \hat{\upsilon}\frac{\partial\overline{p}}{\partial x} - \hat{u}\frac{\partial\overline{u}}{\partial x} - \hat{v}\frac{\partial\overline{u}}{\partial y}\right], \tag{10}
$$

$$
\frac{\partial\hat{v}}{\partial x} = \frac{1}{\overline{u}}\left[i\omega\hat{v} - \overline{v}\frac{\partial\hat{v}}{\partial y} - \overline{\upsilon}\frac{\partial\hat{p}}{\partial y} - \hat{\upsilon}\frac{\partial\overline{p}}{\partial y} - \hat{u}\frac{\partial\overline{v}}{\partial x} - \hat{v}\frac{\partial\overline{v}}{\partial y}\right], \tag{11}
$$

and

$$\frac{\partial \hat{p}}{\partial x} = \frac{1}{\overline{u}}\left[i\omega\hat{p} - \gamma\overline{p}\frac{\partial \hat{u}}{\partial x} - \gamma\overline{p}\frac{\partial \hat{v}}{\partial y} - \overline{v}\frac{\partial \hat{p}}{\partial y} - \hat{u}\frac{\partial \overline{p}}{\partial x} - \hat{v}\frac{\partial \overline{p}}{\partial y} - \gamma\hat{p}\left(\frac{\partial \overline{u}}{\partial x} + \frac{\partial \overline{v}}{\partial y}\right)\right]. \tag{12}$$

However, there are circular dependencies in Eqns. 9 through 12 between the unknown streamwise derivative terms. Substituting the energy equation into the x-momentum equation and simplifying removes circular dependencies and results in

$$\frac{\partial \hat{u}}{\partial x} = \frac{i\omega(\overline{u}\hat{u} - \overline{\upsilon}\hat{p}) + \overline{\upsilon}\gamma\overline{p}\frac{\partial \hat{v}}{\partial y} + \overline{\upsilon v}\frac{\partial \hat{p}}{\partial y} - \overline{uv}\frac{\partial \hat{u}}{\partial y} - \hat{u}\frac{\partial \overline{p}}{\partial x} - \hat{v}\frac{\partial \overline{p}}{\partial y} + \gamma\hat{p}\left(\frac{\partial \overline{u}}{\partial x} + \frac{\partial \overline{v}}{\partial y}\right) + \hat{\upsilon}\frac{\partial \overline{p}}{\partial x} + \hat{u}\frac{\partial \overline{u}}{\partial x} + \hat{v}\frac{\partial \overline{u}}{\partial y}}{\overline{u}^2 - \overline{\upsilon}\gamma\overline{p}}. \tag{13}$$

These equations are represented as an x-continuous integration problem as

$$\frac{d\hat{\boldsymbol{q}}}{dx} = \boldsymbol{\psi}\hat{\boldsymbol{q}}, \tag{14}$$

where $\hat{\boldsymbol{q}}$ is the Fourier transformed vector of perturbation flow variables and $\boldsymbol{\psi}$ represents the matrix of cross-flow discretization coefficients.

Spatially integrating this set of governing equations are valid for supersonic base flows as the system is hyperbolic. For subsonic flow in a boundary layer, this system is ill-posed. For a well-posed system for spatial integration, characteristics with upstream group velocity must be removed [8]. Our CHAOS solver, based on Eqn. 14, requires Fourier transformed fluctuation variables of pressure, specific volume, and velocity at the inlet plane.

B. Numerical Solution Approach

The Dispersion Relation Preserving (DRP) scheme, originally devised by Tam and Webb [19] with further improvements and expanded stencils undertaken by Zhuang and Chen [20], is implemented into CHAOS. DRP is chosen as a spatial discretization scheme because coefficients are optimized to minimize the difference between modified wavenumbers and exact wavenumbers. This is crucial due to the need of accurately resolving acoustic modes, which has been a challenge to capture for previous spatial marching approaches [7]. Consider the finite difference approximation of a derivative of quantity, F:

$$\frac{\partial F}{\partial x} \approx \frac{1}{\Delta x}\sum_{j=-N}^{M} a_j F(x + j\Delta x). \tag{15}$$

In the DRP scheme of Tam and Webb [19], the Fourier transform of the finite-difference approximation will retain the spatial wavenumbers of the continuous derivative. The optimal coefficients, a_j, are provided by Zhuang and Chen [20] for the 7-point scheme and Bogey and Bailly [21] for the 13-point scheme.

Equations 9, 11, 12, and 13 are integrated in the streamwise direction with a Continuous-Stage Runge-Kutta (csRK) algorithm, which increases the formal order of accuracy of the method with respect to step-size. In the present extended abstract, CHAOS retains global 4^{th}-order accuracy. The coefficients in the csRK scheme employed are not optimized for minimization of dispersion error.

Numerical instability of streamwise integration occurs due to upstream traveling modes [8]. Characteristics along the streamwise axis are locally obtained by diagonalizing the LNS Jacobian acting on streamwise derivatives, such that

$$\boldsymbol{A} = \boldsymbol{T}\tilde{\boldsymbol{A}}\boldsymbol{T}^{-1}, \tag{16}$$

where eigenvalue and eigenvector matrices $\tilde{\boldsymbol{A}}$ and $\boldsymbol{T}$, respectively, are

$$\tilde{\boldsymbol{A}} = \begin{bmatrix} \overline{u} & 0 & 0 & 0 \\ 0 & \overline{u} & 0 & 0 \\ 0 & 0 & \overline{u} - \overline{c} & 0 \\ 0 & 0 & 0 & \overline{u} + \overline{c} \end{bmatrix}, \tag{17}$$

and

$$\boldsymbol{T} = \begin{bmatrix} 0 & 1 & -\frac{\overline{v}}{\gamma\overline{p}} & -\frac{\overline{v}}{\gamma\overline{p}} \\ 0 & 0 & -\sqrt{\frac{\overline{v}}{\gamma\overline{p}}} & \sqrt{\frac{\overline{v}}{\gamma\overline{p}}} \\ 1 & 0 & 0 & 0 \\ 0 & 0 & 1 & 1 \end{bmatrix}. \tag{18}$$

Characteristics associated with $\overline{u} - \overline{c}$ wave speeds are destabilizing for spatial integration and drives the requirement for a minimum step size in previous PSE formulations [1, 8]. In the present explicit approach, generalized in Alg. 1, we eliminate the upstream traveling mode at the current marching plane before cross-flow discretization and integration to the next plane. Within the loops for streamwise integration and cross-flow discretization, the solver checks the local Mach number of the base flow. If the flow is locally subsonic, the solution vector, $\boldsymbol{q}$, is transformed to characteristic space and the characteristic associated with $\overline{u} - \overline{c}$ wave speed is removed. Then, the characteristic vector is transformed back to primitive variable space and the spatial integration continues. For local supersonic flow, the characteristic associated with $\overline{u} - \overline{c}$ wave speed is downstream traveling. Thus, the filtering algorithm is locally bypassed.

Algorithm 1 Algorithm for Upstream Characteristic Filtering.

for $i = 1$ to N **do**
  Spatial integration in streamwise direction
  for $j = 1$ to M **do**
    if $M(i, j) < 1$ **then**
      Transform to characteristic space
      $\boldsymbol{\phi} \leftarrow \boldsymbol{T}\hat{\boldsymbol{q}}$
      $\boldsymbol{A} \leftarrow \boldsymbol{T}\tilde{\boldsymbol{A}}\boldsymbol{T}^{-1}$
      $\boldsymbol{B} \leftarrow \boldsymbol{T}\tilde{\boldsymbol{B}}\boldsymbol{T}^{-1} + \tilde{\boldsymbol{A}}\boldsymbol{T}\frac{\partial \boldsymbol{T}^{-1}}{\partial x}$
      Eliminate upstream group velocity characteristics
      $\hat{\phi}(\overline{u} - \overline{c} < 0) \leftarrow 0$
      $\hat{\boldsymbol{q}} \leftarrow \boldsymbol{T}^{-1}\hat{\boldsymbol{\phi}}$
    else
      Continue
    end if
    Discretize cross-flow derivatives
    Apply boundary conditions
  end for
end for

III. Results

We present validation cases for one and two dimensions. We consider the linearized Euler equations (LEE), such that $\boldsymbol{D} = \boldsymbol{0}$. One-dimensional predictions are compared with analytical plane wave solutions to demonstrate accuracy of the spatial integration scheme. Two-dimensional validation using superpositions of periodic-convecting monopoles are presented to further explore two-dimensional solutions. Furthermore, we validate the implementation of a slip-wall boundary condition with the half-space convecting monopole solution of Ochmann [22] for the future application of CHAOS to hypersonic boundary layers.

A. Analytical Solutions

For a one-dimensional wave traveling in a stationary medium, there is only one solution corresponding to the $\overline{u} + \overline{c}$ characteristic, and is

$$\hat{p} = \cos\left(\frac{fx}{\overline{u} + c_\infty}\right). \tag{19}$$

For a two-dimensional periodic convecting monopole, the exact solution for pressure fluctuations in the frequency domain, as given by Ochmann [22], is

$$\hat{p} = R^{-1/2} \exp\left[ik\gamma_k^2 R_1\right] \exp\left[-ik\gamma_k^2 Mx\right], \tag{20}$$

where $k = \omega c^{-1}$ and $\gamma_k = \frac{1}{\sqrt{1-M^2}}$. The velocity-dependent source radius, R_1, is

$$R_1 = \sqrt{x^2 + \frac{y^2}{\gamma_k^2}}. \tag{21}$$

The analytical pressure gradients in the streamwise and cross-stream directions are

$$\frac{\partial \hat{p}}{\partial x} = \left[jk\gamma_k^2\left(\frac{x}{R_1} - M\right) - \frac{x}{R_1}\right]\hat{p} \tag{22}$$

and

$$\frac{\partial \hat{p}}{\partial y} = \left[jk\gamma_k^2\left(\frac{x}{R_1} - M\right) - \frac{y}{\gamma_k R_1}\right]\hat{p}, \tag{23}$$

respectively.

Moving pressure gradient terms to the right-hand side in the linearized momentum equations with a parallel flow assumption ($\overline{v} = 0$), back substituting, and solving for $\hat{u}$ and $\hat{v}$, we obtain

$$\hat{u} = \frac{-\frac{\partial \hat{p}}{\partial x}}{\rho_\infty\left[\overline{u}\left(ik\gamma_k^2\left(\frac{x}{R_1} - M\right) - \frac{x}{R_1}\right) - i\omega\right]} \tag{24}$$

and

$$\hat{v} = \frac{-\frac{\partial \hat{p}}{\partial y}}{\rho_\infty\left[\overline{u}\left(ik\gamma_k^2\left(\frac{x}{R_1} - M\right) - \frac{y}{\gamma_k R_1}\right) - i\omega\right]}. \tag{25}$$

B. One-Dimensional Plane Wave

CHAOS is first validated in one-dimension before its cross-flow capabilities are assessed. Plane waves are propagated in a two-dimensional rectangular domain, with dimensions of 100×1 m^2 and symmetric boundaries for hypersonic Mach numbers ($5 \leq M_\infty \leq 11$). A two-dimensional domain is chosen for one-dimensional validation to ensure the implementation of cross-flow discretization remains zero for plane waves. The grid resolution is approximately 115 points per wavelength in the axial direction and 200 grid points in the cross-stream direction. Extreme grid resolution is chosen to minimize numerical dispersion errors during initial validation of the solver.

Validation for the one-dimensional capability of the solver with Eqn. 19 is completed for a uniform base flow at freestream Mach numbers of 5, 7, 9, and 11. Figures 1a through 1d show predictions of the plane wave from $x = 0$ to 100 m, approximately 30 wavelengths downstream. Ambient conditions include: $\rho_\infty = 0.019$ kg m^{-3}, $T_\infty = 62.0$ K, and $\omega = 300$ rad s^{-1} [23]. For these cases, cross-flow derivatives are zero. A line is extracted in the center of the domain for $\hat{\boldsymbol{q}} - x$ in the axial direction. From $x = 0$ to $x = 10$ m shown in Figs. 1a and 1b, there is excellent agreement in predicted real pressure and velocity perturbations compared with the exact solution shown in Eqn. 19. Extending approximately 30 wavelengths downstream, the predictions show excellent agreement with the exact solution, with an L_2-norm error of 1.48 for $M_\infty = 5$, 1.36 for $M_\infty = 7$, 1.09 for $M_\infty = 9$, and 0.91 for $M_\infty = 11$. There is inherent phase error in the solution due to the integration scheme used not containing optimal coefficients for modified wavenumber minimization [21].

C. Convecting Subsonic Acoustic Monopole

Multiple periodic convecting monopoles are considered in two dimensions. For these cases, the first monopole is placed 40 m to the left of the inlet plane at $y = 0$. The second monopole is placed at the same location in x, but varies in the positive y-direction from 2 m to 40 m. The inlet boundary condition of the solver is calculated from Eqns. 20 through 25 at $x = 0$. Mirrored boundary conditions are used at the cross-flow boundaries. Boundary conditions are applied on the fluid fluctuation variables instead of the characteristics, causing unwanted wave reflections. Such unwanted wave reflections can be removed by applying radiation boundary conditions to incoming Riemann invariants and extrapolating outgoing waves [24]. The filtering algorithm used in these cases features linear extrapolation of the upstream traveling characteristic.

Figures 2a and 2b show the magnitude of pressure fluctuations, and Figs. 2c and 2d show the real part of pressure fluctuations. There is qualitative agreement between predicted contours of $\Re(\hat{p})$ and the analytical solution. Predictive error relative to the analytical solution is quantified along a line extraction at $y = 0$, as shown in Fig. 3a. Figures 3a and 3b show these comparisons for freestream Mach numbers of 0.2, 0.5, 0.6, and 0.7. Predictions are shown as a solid black line, and the analytical solution is represented as non-solid red, blue, purple, or green lines, respectively for $M_\infty = 0.2, 0.5, 0.6$, and 0.7. Overall, the relative error between predicted peak wave amplitudes and the peak wave amplitudes determined by Eqn. 20 is less than one percent. The L_2-norm relative errors between predicted $\Re(\hat{p})$ and the analytical solution for $M_\infty = 0.2, 0.5, 0.6$, and 0.7, are: 0.51, 0.67, 0.81, and 0.86, respectively. Phase error in the streamwise direction is reduced by decreasing the marching step-size.

We present an expanded set of validation cases for dual periodic convecting monopoles for frequencies up to 40×10^3 rad s^{-1}. The first monopole is located at $x = -40$ and $y = 0$ m from the inlet plane origin. However, the second monopole is placed within $y = 2$ m to $y = 30$ m of the origin. This is done to assess the capability of CHAOS to handle larger cross-flow wavenumbers associated the resultant interference patterns. Figures 4 through 10 show these extended validation cases. Overall, the predictions show good agreement with the analytical solution, with the worst case being when the two sources are 30 m apart. This case, shown in Figs. 5a and 5b shows an over-prediction in wave magnitude compared to the analytical solution. This is because the inlet is near the limit of the downstream traveling cone of influence for the monopole placed at $x = -40$ and $y = 30$ m. For $M_\infty = 0.6$, the cone of influence for the downstream traveling characteristic is 30.005 deg. This corresponds to the inlet center location featuring downstream-only characteristics, which are located within 48 m in the downstream direction. The filtering algorithm in CHAOS removes the upstream traveling modes, affecting the prediction of wave magnitude.

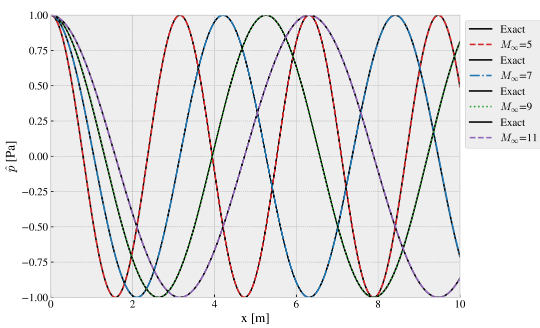

(a) Real part of pressure fluctuation.

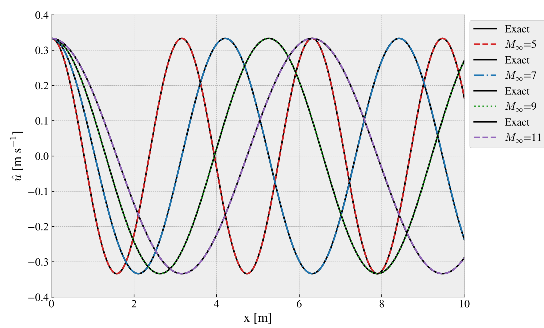

(b) Real part of axial velocity fluctuation.

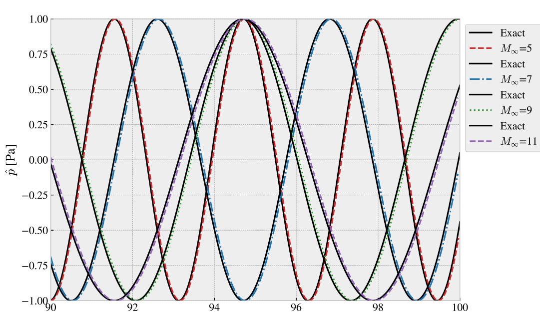

(c) Real part of pressure fluctuation.

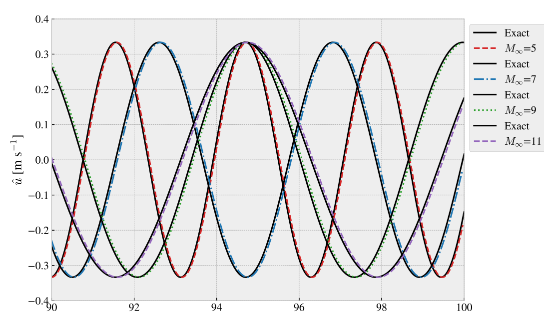

(d) Real part of axial velocity fluctuation.

Fig. 1 Predictions of plane waves in a high-speed base flow from 0 to 100 m for first (top) and final (bottom) three wavelengths inside the domain.

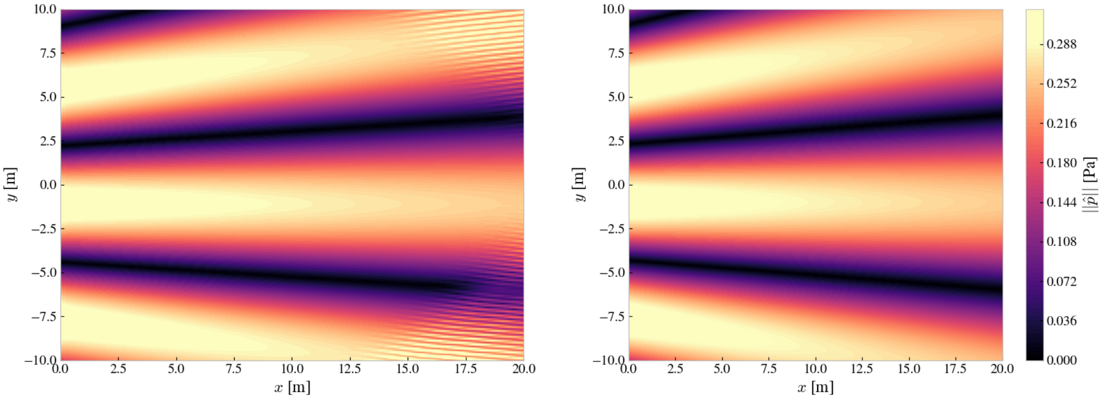

(a) CHAOS. **(b) Analytical.**

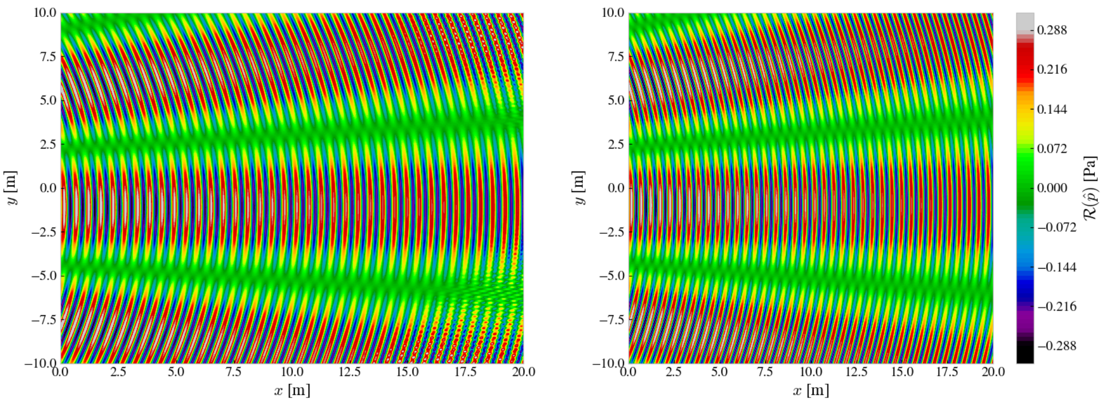

(c) CHAOS. **(d) Analytical.**

Fig. 2 Validation with superposition of periodic-convecting monopoles placed 2.0 **m apart in the vertical direction for real-part (top) and amplitude (bottom) of pressure fluctuations at** $M_\infty = 0.6$, $\omega = 30 \times 10^3$ **rad s**$^{-1}$**, and** $x_{\text{source}} = -40$ **m.**

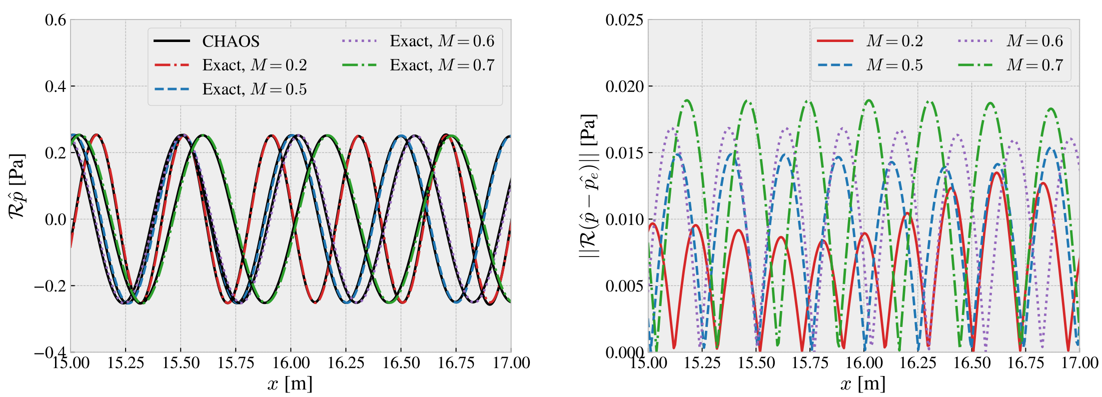

(a) $\Re(\hat{p})$ **along the centerline of the domain.** **(b) Absolute value of error for** $\Re(\hat{p})$**.**

Fig. 3 Comparison between predicted and analytical $\Re(\hat{p})$ **(left) along the line** $y = 0$ **with corresponding relative error (right) at** $\omega = 30 \times 10^3$ **rad s**$^{-1}$**, and** $x_{\text{source}} = -40$ **m.**

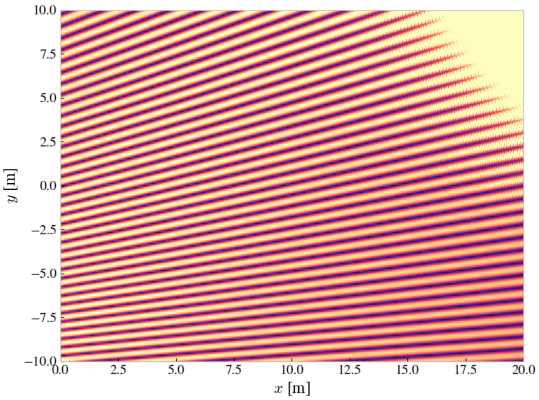

(a) CHAOS.

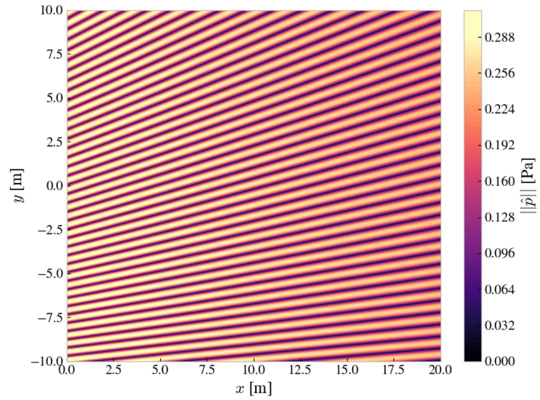

(b) Analytical.

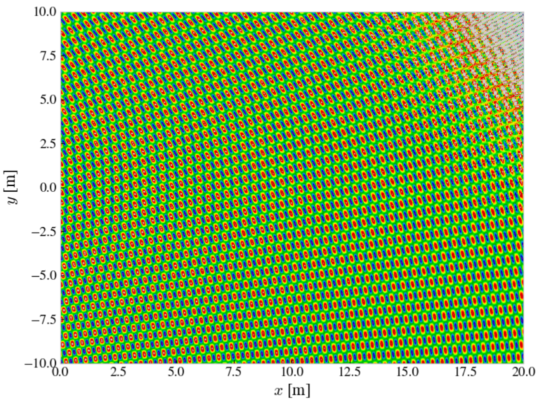

(c) CHAOS.

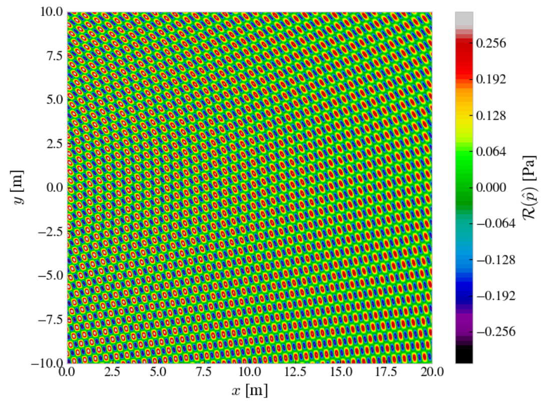

(d) Analytical.

Fig. 4 Validation with superposition of periodic-convecting monopoles placed 30.0 **m apart in the vertical direction for real-part (top) and amplitude (bottom) of pressure fluctuations at** $M_\infty = 0.2$**,** $\omega = 30 \times 10^3$ **rad s**$^{-1}$ **and** $x_{\mathbf{source}} = -40$ **m.**

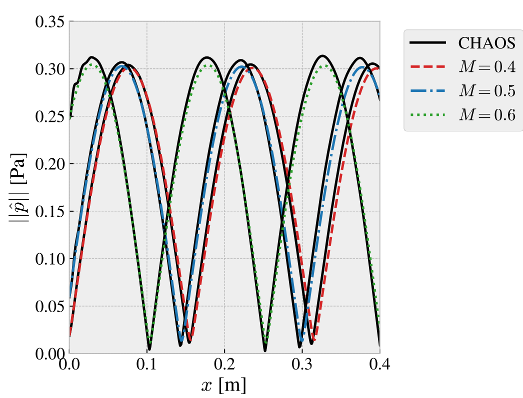

(a) $||\hat{p}||$**.**

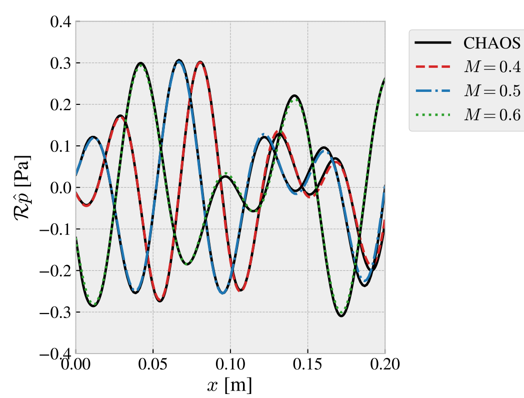

(b) $\Re(\hat{p})$**.**

Fig. 5 Centerline extractions of superpositions of periodic-convecting monopoles placed 30.0 **m apart in the vertical direction at** $\omega = 30 \times 10^3$ **rad s**$^{-1}$ **and** $x_{\mathbf{source}} = -40$ **m.**

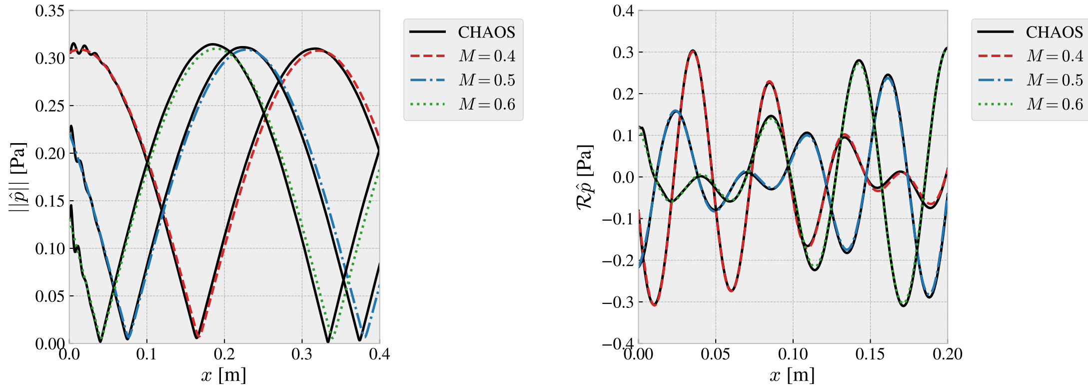

(a) $||\hat{p}||$. **(b)** $\Re(\hat{p})$.

Fig. 6 Centerline extractions of superpositions of periodic-convecting monopoles placed 20.0 **m apart in the vertical direction at** ω = 30 × 10^3 **rad s**$^{-1}$ **and** x_{source} = −40 **m.**

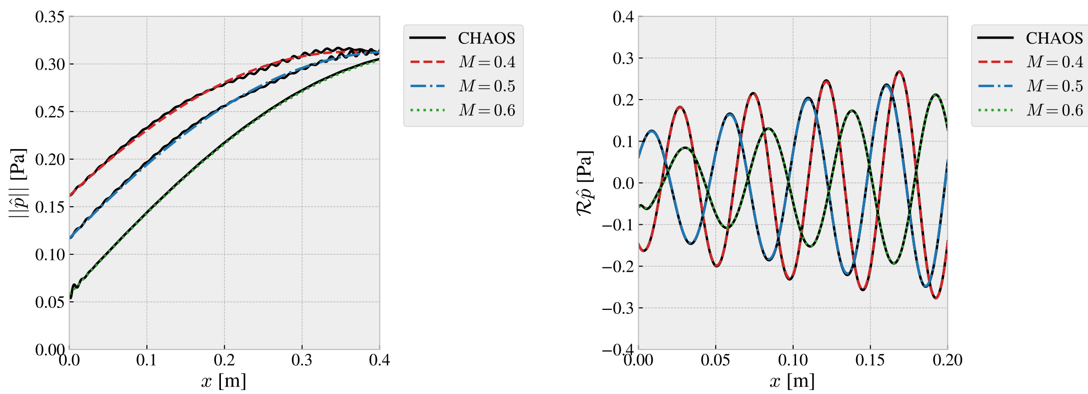

(a) $||\hat{p}||$. **(b)** $\Re(\hat{p})$.

Fig. 7 Centerline extractions of superpositions of periodic-convecting monopoles placed 10.0 **m apart in the vertical direction at** ω = 30 × 10^3 **rad s**$^{-1}$ **and** x_{source} = 40 **m.**

D. Wall Boundary Condition

The wall boundary condition is validated with the dual half-space solution Ochmann [22]. There is no impedance included in the initial condition at the wall. The initial condition is formed by evaluating two monopoles, with the first source placed 1 m above the wall and the second source placed 1 m below the wall. Both monopoles are placed 60 m upstream of the inlet. A slip-wall boundary condition is enforced. The computational domain extends from 0 m ≤ x ≤ 1 m and 0 m ≤ y ≤ 2 m.

Figure 11 shows the contours of real pressure perturbation for the half-space monopole case with a slip-wall. In particular, for Figs. 12b through 12c, the error between the CHAOS-predicted solution relative to the analytical solution grows with freestream Mach number. This is due to the amplification of phase error with axial mean velocity. As mean velocity increases, the phase error of the predicted solution also increases. Maximum absolute error, normalized by freestream pressure is $Ep_\infty^{-1} = 0.000675$ and occurs at $M_\infty = 0.9$ and $x = 0.144$ m for 15.9 kHz. Unexpectedly, error for 15.9 kHz was larger than the highest frequency case at 79.6 kHz.

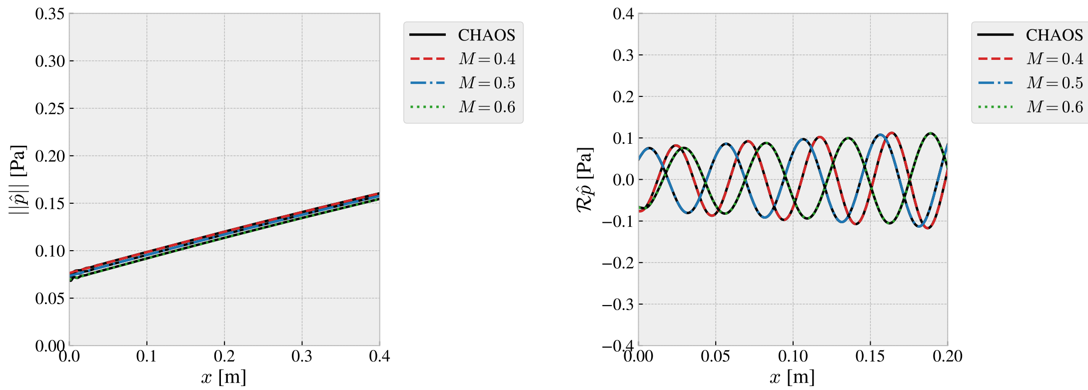

(a) $||\hat{p}||$. **(b)** $\Re(\hat{p})$.

Fig. 8 Centerline extractions of superpositions of periodic-convecting monopoles placed 5.0 **m apart in the vertical direction at** $\omega = 30 \times 10^3$ **rad s**$^{-1}$ **and** $x_{\textbf{source}} = -40$ **m.**

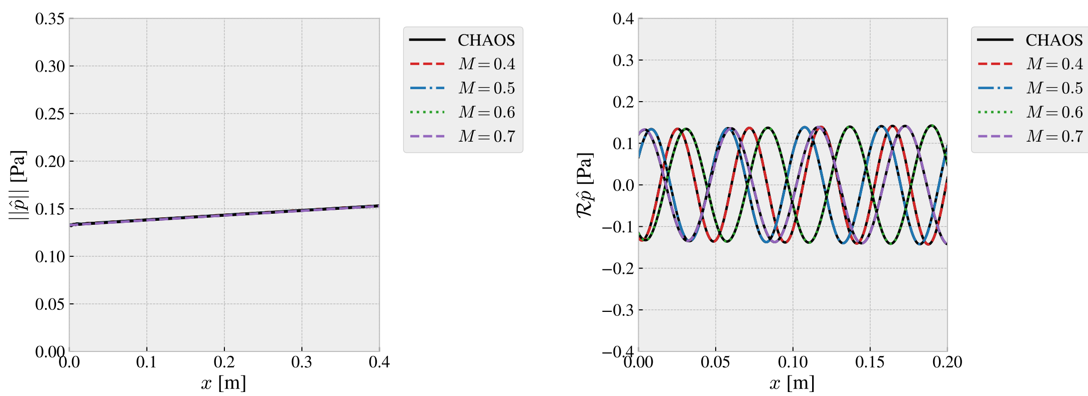

(a) $||\hat{p}||$. **(b)** $\Re(\hat{p})$.

Fig. 9 Centerline extractions of superpositions of periodic-convecting monopoles placed 2.5 **m apart in the vertical direction at** $\omega = 30 \times 10^3$ **rad s**$^{-1}$ **and** $x_{\textbf{source}} = -40$ **m.**

IV. Summary and Conclusion

A new high-order, explicit one-way instability methodology and computer program are introduced. For local subsonic flow, the equations of motion are parabolized by eliminating characteristic variables associated with upstream group velocity. The parabolized set of equations are integrated in the streamwise direction with a csRK method using a 7- or 13-point central DRP discretization scheme in the cross-flow direction. We present validation cases of one-dimensional plane waves and superpositions of periodic convecting monopoles for supersonic and subsonic base flows, respectively. For quasi-1D planar acoustic wave validation cases, hypersonic Mach numbers are swept from 5 through 11. Overall, peak wave amplitude for all cases is less than 1% of the examined analytical solutions at approximately 30 wavelengths downstream. In two dimensions, predictions of dual periodic convecting monopoles in subsonic flow are compared with the free-space analytical solution of Ochmann [22]. We demonstrate validation of a slip-wall boundary condition with a half-space periodic convecting monopole.

In the future, we will conduct predictions of planar and periodic monopole forcing within hypersonic boundary layers. CHAOS will be further developed to investigate the effects of freestream forcing on boundary layers at Mach numbers ranging from 4.5 to 7.4 [25]. We also look to implement the base flow cases of Sousa et al. [26] and Wartemann et al. [27] for flat plates and sharp cones.

Acknowledgments

This material is based upon work supported by the National Science Foundation Graduate Research Fellowship under Grant No. AWD13127-2236414. Any opinion, findings, and conclusions or recommendations expressed in this material are those of the authors(s) and do not necessarily reflect the views of the National Science Foundation.

The authors' are indebted for extensive discussions with Dr. Meelan Choudhari of NASA Langley Research Center.

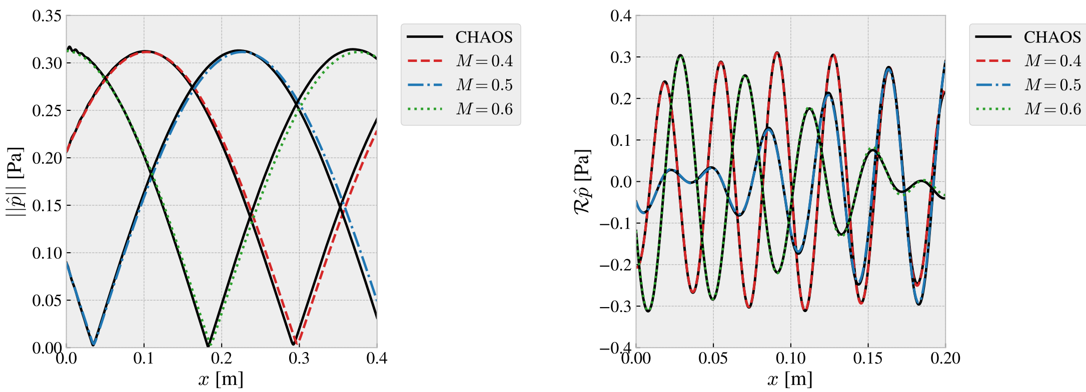

(a) $||\hat{p}||$.

(b) $\Re(\hat{p})$.

Fig. 10 Centerline extractions of superpositions of periodic-convecting monopoles placed 15 **m apart in the vertical direction at** $\omega = 40 \times 10^3$ **rad** $\mathbf{s}^{-1}$ **and** $x_{\textbf{source}} = -40$ **m.**

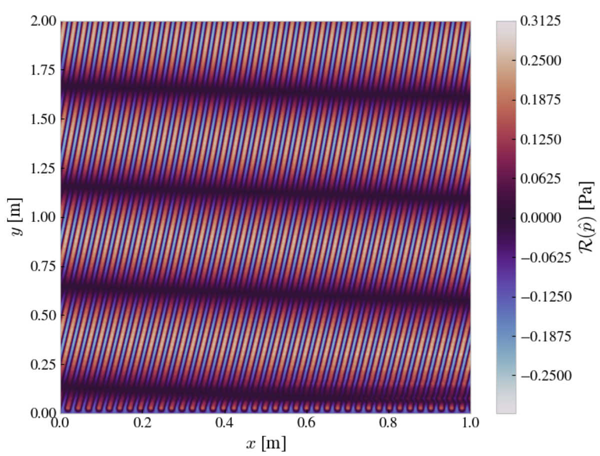

Fig. 11 Contours of real pressure perturbations of pressure along with wall for a temporal frequency of 9.5 **kHz.**

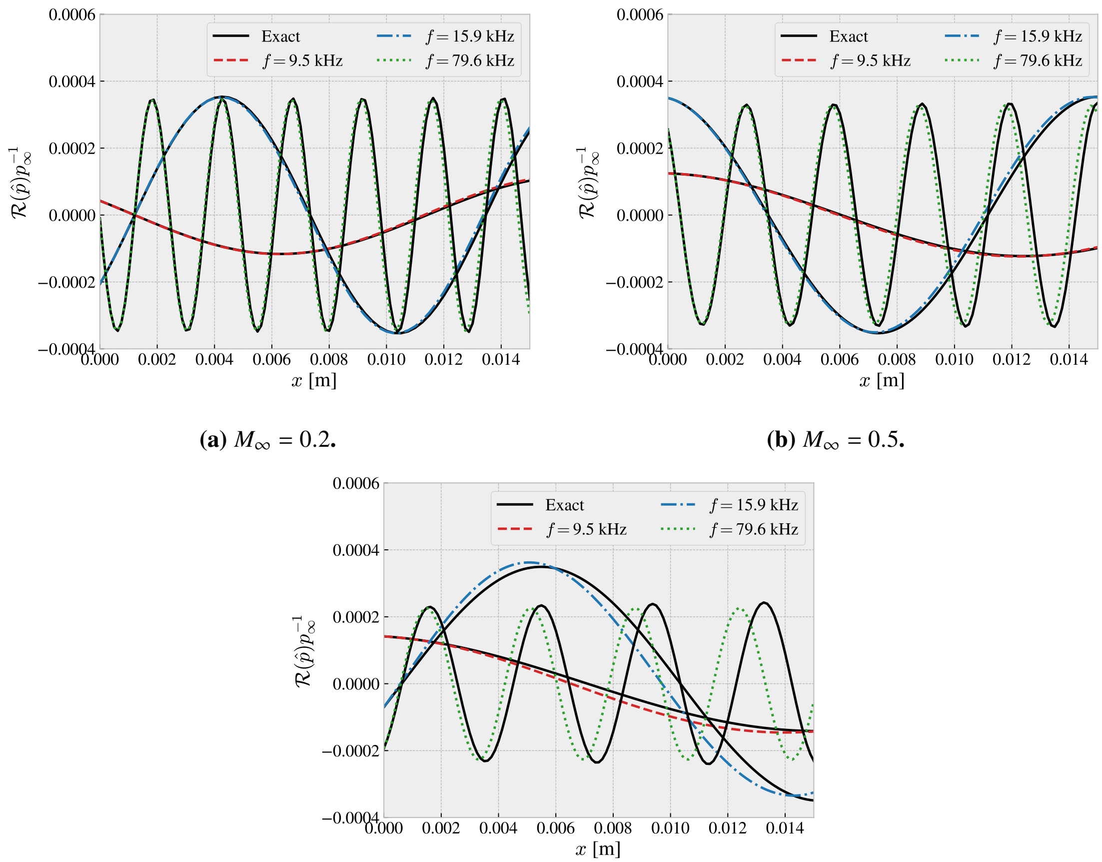

(a) $M_\infty = 0.2$**.**

(b) $M_\infty = 0.5$**.**

(c) $M_\infty = 0.9$**.**

Fig. 12 Real pressure perturbations of pressure along with wall for temporal frequencies of 9.54**,** 15.9**, and** 79.6 **kHz, respectively.**

References

[1] Li, F., and Malik, M. R., "On the nature of PSE approximation," *Theoretical and Computational Fluid Dynamics*, Vol. 8, No. 4, 1996, pp. 253–273. doi:10.1007/BF00639695.

[2] Lawrence, S. L., Tannehill, J. C., and Chausee, D. S., "Upwind Algorithm for the Parabolized Navier-Stokes Equations," *AIAA Journal*, Vol. 27, No. 9, 1989, pp. 1175–1183. doi:10.2514/3.10243.

[3] Miller, J. H., Tannehill, J. C., and Lawrence, S. L., "Parabolized Navier-Stokes Algorithm for Solving Supersonic Flows with Upstream Influences," *AIAA Journal*, Vol. 38, No. 10, 2000, pp. 1837–1845. doi:10.2514/2.865.

[4] Tannehill, J., Buelow, P., Ievalts, J., and Lawrence, S., "A Three-Dimensional Upwind Parabolized Navier-Stokes Code for Real Gas Flows," *24th Thermophysics Conference*, American Institute of Aeronautics and Astronautics, AIAA Paper 1989-1651, 1989. doi:10.2514/6.1989-1651.

[5] Kendall, J. M., "Wind tunnel experiments relating to supersonic and hypersonic boundary-layer transition," *AIAA Journal*, Vol. 13, No. 3, 1975, pp. 290–299. doi:10.2514/3.49694.

[6] Tollmien, W., "Über Die Entstehung Der Turbulenz (About the Origin of Turbulence)," *Vorträge aus dem Gebiete der Aerodynamik und verwandter Gebiete: Aachen 1929*, 1930, pp. 18–21.

[7] Towne, A., Rigas, G., and Colonius, T., "A Critical Assessment of the Parabolized Stability Equations," *Theoretical and Computational Fluid Dynamics*, Vol. 33, 2019, pp. 359–382. doi:10.1007/s00162-019-00498-8.

[8] Towne, A., and Colonius, T., "One-way spatial integration of hyperbolic equations," *Journal of Computational Physics*, Vol. 300, 2015, pp. 844–861. doi:10.1016/j.jcp.2015.08.015.

[9] Rigas, G., Schmidt, O. T., Colonius, T., and Bres, G. A., "One way Navier-Stokes and resolvent analysis for modeling coherent structures in a supersonic turbulent jet," *23rd AIAA/CEAS Aeroacoustics Conference, Denver, Colorado*, AIAA Paper 2017-4046, 2017. doi:10.2514/6.2017-4046.

[10] Zhu, M., and Towne, A., "Recursive one-way Navier-Stokes equations with PSE-like cost," *Journal of Computational Physics*, Vol. 473, 2023, p. 111744. doi:10.1016/j.jcp.2022.111744.

[11] Towne, A., Rigas, G., Kamal, O., Pickering, E., and Colonius, T., "Efficient global resolvent analysis via the one-way Navier–Stokes equations," *Journal of Fluid Mechanics*, Vol. 948, 2022, p. A9. doi:10.1017/jfm.2022.647.

[12] Bertolotti, F. P., Herbert, T., and Spalart, P., "Linear and nonlinear stability of the Blasius boundary layer," *Journal of fluid mechanics*, Vol. 242, 1992, pp. 441–474. doi:10.1017/S0022112092002453.

[13] Paredes, P., Choudhari, M. M., Li, F., and Chang, C.-L., "Transient growth analysis of compressible boundary layers with parabolized stability equations," *54th AIAA Aerospace Sciences Meeting, San Diego, California*, AIAA Paper 2016-0051, 2016. doi:10.2514/6.2016-0051.

[14] Paredes, P., Hanifi, A., Theofilis, V., and Henningson, D. S., "The nonlinear PSE-3D concept for transition prediction in flows with a single slowly-varying spatial direction," *Procedia IUTAM*, Vol. 14, 2015, pp. 36–44. doi:10.1016/j.piutam.2015.03.021.

[15] Hermanns, M., and Hernandez, J. A., "Stable high-order finite-difference methods based on non-uniform grid point distributions," *International journal for numerical methods in fluids*, Vol. 56, No. 3, 2008, pp. 233–255. doi:10.1002/fld.1510.

[16] Gaster, M., "A note on the relation between temporally-increasing and spatially-increasing disturbances in hydrodynamic stability," *Journal of Fluid Mechanics*, Vol. 14, No. 2, 1962, pp. 222–224.

[17] Gaster, M., "Growth of disturbances in both space and time," *The Physics of Fluids*, Vol. 11, No. 4, 1968, pp. 723–727.

[18] Rigas, G., Colonius, T., and Beyar, M., "Stability of wall-bounded flows using one-way spatial integration of Navier-Stokes equations," *55th AIAA Aerospace Sciences Meeting, Grapevine, Texas*, AIAA Paper 2017-1881, 2017. doi:10.2514/6.2017-1881.

[19] Tam, C. K., and Webb, J. C., "Dispersion-relation-preserving finite difference schemes for computational acoustics," *Journal of computational physics*, Vol. 107, No. 2, 1993, pp. 262–281. doi:10.1006/jcph.1993.1142.

[20] Zhuang, M., and Chen, R., "Optimized upwind dispersion-relation-preserving finite difference scheme for computational aeroacoustics," *AIAA Journal*, Vol. 36, No. 11, 1998, pp. 2146–2148. doi:10.2514/2.319.

[21] Bogey, C., and Bailly, C., "A family of low dispersive and low dissipative explicit schemes for flow and noise computations," *Journal of Computational physics*, Vol. 194, No. 1, 2004, pp. 194–214. doi:10.1016/j.jcp.2003.09.003.

[22] Ochmann, M., “Exact solutions for sound radiation from a moving monopole above an impedance plane,” *The Journal of the Acoustical Society of America*, Vol. 133, No. 4, 2013, pp. 1911–1921. doi:10.1121/1.4794389.

[23] Lockman, W. K., Lawrence, S. L., and Cleary, J. W., “Flow Over an All-Body Hypersonic Aircraft-Experiment and Computation,” *Journal of Spacecraft and Rockets*, Vol. 29, No. 1, 1992, pp. 7–15. doi:10.2514/3.26308.

[24] Sommerfeld, A., *Ein beitrag zur hydrodynamischen erklaerung der turbulenten fluessigkeitsbewegungen (A contribution to the hydrodynamic explanation of turbulent fluid movements)*, Proceedings of the 4th International Congregation of Mathematics, Accademia dei Lincei, Rome, 1909.

[25] Kamal, O., Rigas, G., Lakebrink, M. T., and Colonius, T., “Application of the One-Way Navier-Stokes (OWNS) equations to hypersonic boundary layers,” *AIAA Aviation 2020 Forum, Virtual*, AIAA Paper 2020-2986, 2020. doi:10.2514/6.2020-2986.

[26] Sousa, V. C., Patel, D., Chapelier, J.-B., Wartemann, V., Wagner, A., and Scalo, C., “Numerical investigation of second-mode attenuation over carbon/carbon porous surfaces,” *Journal of Spacecraft and Rockets*, Vol. 56, No. 2, 2019, pp. 319–332. doi:10.2514/1.A34294.

[27] Wartemann, V., Wagner, A., Kuhn, M., Eggers, T., and Hannemann, K., “Passive Hypersonic Boundary Layer Transition Control Using an Ultrasonically Absorptive Coating With Random Microstructure: Computational Analysis Based on the Ultrasonic Absorption Properties of Carbon-Carbon,” *Procedia IUTAM*, Vol. 14, 2015, pp. 413–422. doi:10.1016/j.piutam.2015.03.068.